CrystEngComm

Modified Floating-Zone Crystal Growth of Mg4Ta2O9 and Its Scintillation Performance

Journal:	*CrystEngComm*
Manuscript ID	CE-ART-03-2020-000388.R1
Article Type:	Paper
Date Submitted by the Author:	01-May-2020

Complete List of Authors:	Yuan, Dongsheng; Lawrence Berkeley National Laboratory Moretti, Federico; Lawrence Berkeley National Laboratory Perrodin, Didier; Lawrence Berkeley National Laboratory Bizarri, Gregory; Lawrence Berkeley National Laboratory; Cranfield University Shalapska, Tetiana; Lawrence Berkeley National Laboratory Dujardin, Christophe; University Claude Bernard Lyon 1, Institut Lumière Matière Bourret, Edith; Lawrence Berkeley National Laboratory,

ARTICLE

Modified Floating-Zone Crystal Growth of $Mg_4Ta_2O_9$ and Its Scintillation Performance

Received 00th January 20xx,
Accepted 00th January 20xx

DOI: 10.1039/x0xx00000x

Dongsheng Yuan,[a] Federico Moretti,[a] Didier Perrodin,[a] Gregory Bizarri,[a] Tetiana Shalapska,[a] Christophe Dujardin [b] and Edith Bourret *[a]

Aiming to explore scintillator candidates for high-energy radiography, the environmentally friendly compound $Mg_4Ta_2O_9$ was selected. Bulk crystals of good optical quality are needed to evaluate its scintillation performance against other commercial scintillators currently used such as $CdWO_4$ and CsI:Tl. In this work, bulk single crystal rods of 3.5 mm in diameter with length up to 50 mm were obtained through optimization of the growth process. Particularly, the thermal gradients that impact the cooling of the crystal in the floating-zone furnace were modified. The scintillation properties of the produced $Mg_4Ta_2O_9$ crystals, are reported. The scintillation decay and afterglow not reported previously have been measured. The afterglow results are compared to those of $CdWO_4$, CsI:Tl and $Y_3Al_5O_{12}$:Ce. We confirmed a luminosity similar to that of $CdWO_4$.

Introduction

Scintillators work as a spectral and energy transformer converting high-energy particles or X- or γ-ray photons into ultraviolet-visible light [1,2]. Their use in X-ray and nuclear medicine imaging devices is well documented (see for example [3]). For these applications the energy of the detected ranges from a few tens of keV for soft X-ray imaging up to 511keV for PET scanners. Here we are searching for scintillators to be used in imaging devices that uses high energy sources in the MeV range for radiography of large and dense loads such as the loads in cargo container. For high-energy X-ray radiography, inorganic materials with high stopping power (high density), good light yield (>10,000photons/MeV), low afterglow, short decay time are needed [4-6]. In addition, these imaging applications require large amounts of scintillators that should be produced at a reasonable cost. Newly developed crystals should be able to be produced for large arrays of pixels of about 1x1x2cm each. Intrinsic materials avoid the cost of using rare-earth activators and avoid scintillation response inhomogeneities related to dopant segregation. Some of the materials that have attractive properties for this application, such as $(Y, Gd)_2O_3$:(Eu, Pr, Tb) and Gd_2O_2S:(Pr, Ce, F), can only be fabricated as ceramics [7-9]. The lack in transparency of these materials limits their use to rather thin layers, thus diminishing their ability to absorb fully the incoming X-rays. Single crystal materials commonly employed in high-energy radiography applications are cadmium tungstate ($CdWO_4$) and thallium activated cesium iodide (CsI:Tl). $CdWO_4$ has a good stopping power and almost no afterglow but suffers from a relatively low luminosity [10], and the toxic element Cd poses concerns for its disposal. CsI:Tl (without additional dopants) has a good light yield and stopping power but its large afterglow degrades its performance [11]. It contains Tl which can present a toxicity issue.

This paper follows a previous study reviewing a wide tantalate series from which we selected $Mg_4Ta_2O_9$ for further development [12]. However, that study as well as reports from others [13] showed that all crystals suffered from issues of bubbles formation and cracking, prompting an effort to optimize the growth process. In this work we used the float-zone technique. While very frequently used for growth of oxides with high melting point, the growth process in itself is quite complex and well described in a number of review articles [14-16]. One of the drawback of the technique is the presence of sharp temperature gradients between the molten zone and the growing crystal that can induce thermal stresses on the cooling crystal. The issue has been addressed in a publication for the growth of SiGe alloys by adding an additional heater around the float-zone [17]. In this study, the growth process was improved by modification of a traditional floating-zone furnace using an insulating block below the float-zone to decrease the temperature gradient around the emerging crystal. The cracking and bubbles issues were then resolved and transparent crystal rods, 3.5 mm in diameter and 50 mm long, were obtained and we present their complete scintillation performance.

Experimental

Single Crystal Growth and Structure Determination

Growth method. Single crystals of $Mg_4Ta_2O_9$ were grown in air using an optical floating-zone furnace (Cyberstar) [18,19] as

[a] *Materials Sciences Division and Life Sciences Division, Lawrence Berkeley National Laboratory, 1 Cyclotron Road, Berkeley, CA 94720, USA. Email: edbourret@lbl.gov (E.B.)*
[b] *Université de Lyon, Université Claude Bernard Lyon 1, CNRS, Institut Lumière Matière UMR 5306, F-69622 Villeurbanne, France.*

described in [12]. Two 2000 W Halogen lamps were focused in the center of the quartz chamber by two elliptic mirrors. During crystal growth, feed and seed shafts were counter-rotated at 10 and 30 rpm, respectively, in order to homogenize the molten zone. Both the feed rod and the pull rod have a precision of 0.01mm/hr per manufacturer specifications. The equipment enables pressurization of up to 10 atm. To prevent loss of MgO during growth the air pressure was maintained at 2 atm. A CCD camera was used to record and monitor the crystal growth. The technique is shown schematically in figure 1. Modification to the thermal gradients for this work is explained in next section.

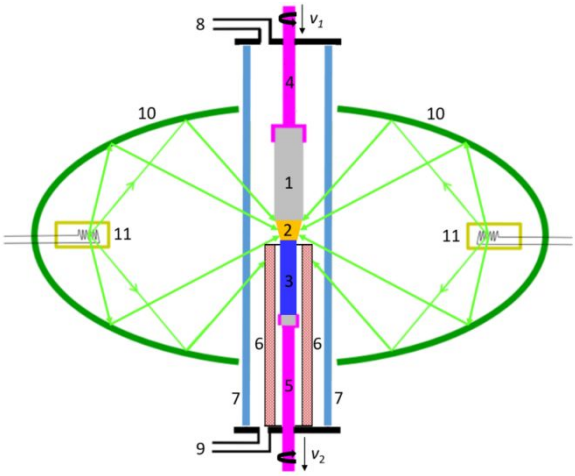

Figure 1: Schematic of the modified floating-zone technique. 1-feeding ceramic rod, 2-molten zone, 3-grown crystal, 4-feeding shaft, 5-growth shaft, 6-thermal insulating tube (Al_2O_3 ceramic), 7-quartz chamber, 8-gas valve and outlet, 9-gas valve and inlet, 10-metal mirrors, 11-halogen lamps, v_1-feeding rate, v_2- growth rate.

Sintering of the Ceramic Rods and Phase Identification. The ceramics used as feed rods for crystal growth were prepared by high-temperature solid-state reactions. Both MgO (Alfa Aesar, 99.99%) and Ta_2O_5 (ALDRICH, 99.99 %) were dried at 120 °C for at least 24 h in air before use. Stoichiometric ratio of MgO and Ta_2O_5 were weighed with an excess of 1% MgO added to control the composition since MgO was found to volatilize during synthesis and crystal growth [20]. The mixture was thoroughly ground using an 8000M mixer mill (SPEX SamplePrep) over 3 h and then isostatically pressed into solid rods at 345 MPa. The rods were sintered in air at 1500 °C for 48 h, then cooled down to room temperature at a rate of 50 °C/h.

The phase purity of the obtained rods was checked with powder x-ray diffraction (PXRD). The diffraction patterns were obtained using a Nonius FR591 water-cooled rotating copper-anode X-ray generator (50 kV, 60 mA) (Bruker AXS Inc., Madison, WI) and a Mar detector plate (Mar USA, Inc., Evanston, IL). The collected 2D images were transformed into a standard 1D diffraction pattern with Fit2D software [21], and then Match package [22] was used to analyze the diffraction pattern.

Single-Crystal Structure. The grown crystals were subjected to single-crystal X-ray diffraction to verify their structure. The data were collected at UC Santa Barbara using a Bruker Kappa APEX II diffractometer using Mo-Kα radiation. The APEX SMART program [23] was used to determine the unit cell parameters and perform data collection (5 s/frame, 0.3 degree/frame for a sphere of diffraction data). Data reduction and integration were processed using the SAINT program [20], followed by empirical absorption correction based on multi-scans. The structure was solved by direct methods and refined with full matrix least-squares methods on F^2 [24,25], and calculations were conducted using the SHELXTL crystallographic software package [26].

Laue back-reflection of X-ray images were acquired to identify the crystalline quality and growth orientation of the obtained crystals [27]. The diffraction images were taken using a Multiwire Laboratories real-time back-reflection Laue camera with a tungsten source operating at 20 kV and 25 mA. Typical distance between the X-ray tube tip and samples is 100 mm.

Scintillation Measurements

X-ray excited luminescence spectrum (XRL), X-ray excited luminescence decay, gamma response (pulse height spectrum, PHM), afterglow and thermally stimulated luminescence (TSL) were all performed using cross-section of the crystal rod about 1.5 mm thick with both sides polished.

X-ray generated from the same setup previously described for PXRD measurement was used to excite the crystal samples, and the luminescence spectra were recorded by a SpectraPro-2150i spectrometer (Acton Research Corp., Acton, MA) coupled to a PIXIS:100B charge-coupled detector (Princeton Instruments, Inc.). The obtained spectra have been corrected for the instrumental response.

TSL measurements were conducted using the above setup with the crystal specimen mounted on the cold finger of a cryogenic refrigerator with a temperature range from 15 K to 300 K. $Mg_4Ta_2O_9$ sample was irradiated under X-ray for 30 min. The heating rate was set to 5 K/min.

X-ray excited luminescence decay times were measured on a pulsed X-ray system consisting of an ultrafast laser (200 fs pulses at 165 kHz), a Hamamatsu N5084 light excited X-ray tube (tungsten anode), a Hamamatsu R3809U-50 microchannel PMT and an Ortec 9307 pico-timing discriminator [28].

Pulse height spectra were acquired on a Hamamtsu R6321-100 photomultiplier tube (PMT) to determine luminosity and energy resolution under the excitation of 662 keV ^{137}Cs γ-ray. The PMT was connected to a Canberra 2005 preamplifier, a Canberra 2022 shaping amplifier and an Ortec EASY-MCA-8K multichannel analyzer. The crystal samples were coupled to the PMT window with Viscasil 600000 (GE) optical grease and covered with layers of PTFE reflecting tape. The light output was estimated by comparison of the photopeak position with that of $Bi_4Ge_3O_{12}$ (3×3.5×1.5 mm^3), $CdWO_4$ (5×5×5 mm^3) and $CaWO_4$ (2×2×1.5 mm^3) reference crystals (similar sizes to the $Mg_4Ta_2O_9$

samples under study), which were measured under the identical condition and taking into account the PMT quantum efficiency for each crystal. The energy resolution (at 662 keV) was calculated based on the full width at half maximum (FWHM) of the photopeak.

The afterglow was measured by exciting the samples with X-rays from a Hamamatsu N5084 light-excited X-ray tube driven by a 405 nm pulsed photodiode (pulse width 30 µs at 50 Hz). A PMA series PMT from PicoQuant with a long-pass edge filter at 450 nm and a fast multichannel analyzer (FAST ComTec) were used to collect the afterglow. In addition to $Mg_4Ta_2O_9$ crystal samples, reference crystals of $CdWO_4$, CsI: Tl and $Y_3Al_5O_{12}$: Ce were also measured.

Results and Discussion

Crystal Growth

Ceramic rods of the pure targeted phase are essential to use as feed rods and their composition was confirmed by PXRD. Figure 2 shows the PXRD pattern of a sintered feed rod compared to the standard diffraction profile of corundum $Mg_4Ta_2O_9$ (ICDD 00-38-1428). All the X-ray Bragg peaks of the reference are present in the pattern of the sintered rod. Series of sintered feed rods were tested and the procedure was determined reproducible.

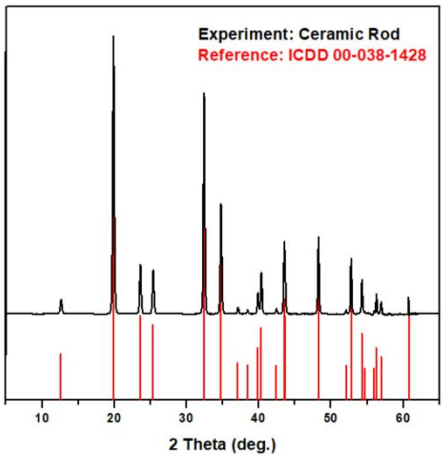

Figure 2. Powder X-ray diffraction pattern of the $Mg_4Ta_2O_9$ ceramic feed rod for crystal growth.

Our previous growth trials indicated that Mg4Ta2O9 has a melting point of over 1800 ˚C and that the best crystal was obtained at a growth rate of 2 mm/h with an overpressure of argon (200 kPa) [13]. This new study confirms the findings. To prepare seed crystals by using ceramic rods (both the feed rod and seed), we translated the molten zone at a speed of 1 mm/h in air. For grain selection, the necking technique was used. The diameter of the rod was decreased to 1.5 mm promoting elimination of some grains at each "neck" before increase the diameter back to 3 mm. After several growth rounds, a single crystal with a length of 12 mm and a diameter of about 3 mm was successfully obtained to be used as a seed. The full-size crystals were then grown seeded. Different growth rates from 0.6 to 3 mm/h were used and the 2 mm/h was confirmed to produce clear crystals. Figure 3(a) shows a crystal rod grown at the rate of 0.6 mm/h. With a pulling rate, smaller than 1 mm/h, the crystals appeared opaque on their surface. Further observation using optical microscopy indicated that opaque particles were not just on the surface, but also embedded into the crystal rods. For a pulling rate of 3 mm/h, even larger white particles were present inside the crystals shown in Figure 3(b). At a growth rate of 2 mm/h, the grown crystals show crystallographic facets with very good transparency. This growth speed was then used in the optimization of the thermal insulation modifications reported below.

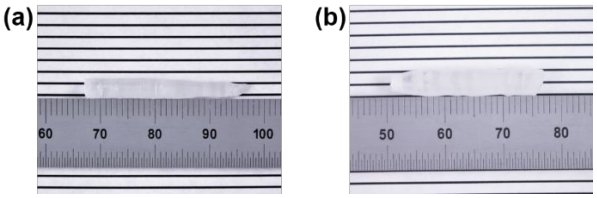

Figure 3. Crystal rods grown using pulling rate of (a) 0.6 mm/h and (b) 3 mm/h, respectively (scale is mm).

While the increased pressure of 200 kPa air and a growth rate of 2 mm/h resulted in transparent faceted crystals, with increasing length, above about 2 cm, the crystals tend to crack longitudinally upon cooling suggesting that a decrease of the thermal stress upon cooling was needed.

The core modification done to the furnace itself to decrease the thermal gradient upon cooling is the addition of an insulating tube inserted in the lower part of the growth chamber (Part#6 in Figure 1). This tube shown in figure 4a below, insulates the crystal and slows down its cooling significantly reducing the thermal stress on the crystal. The shallower and more uniform axial temperature gradient also impacts the solid-liquid interface that becomes less concave. Figure 4(b, c) are images recorded during crystal growth, showing the ceramic-melt-crystal interface and the insulating tube. The growth was ended by increasing the pulling rate and keeping the feeding rate constant to taper the crystal.

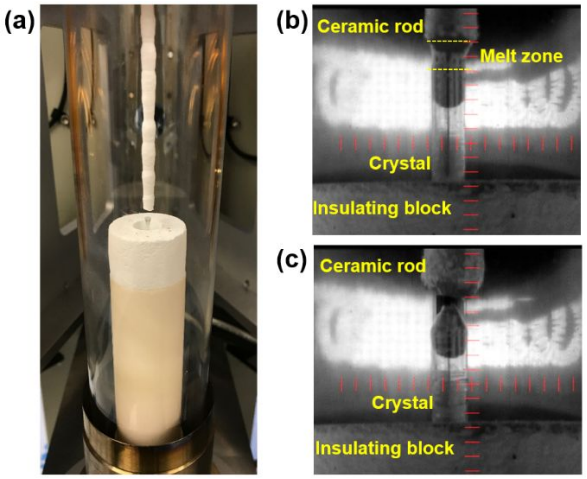

Figure 4. (a) Photograph of the modified setup -insulating tube- inside the quartz growth chamber of our floating-zone furnace.

Real-time ceramic-melt-crystal image recorded at the (b) cylinder and (c) tailing growth stage, respectively. The red bars show 1.5 mm as scale.

More stable crystal growth was then achieved and crack-free crystals more than 50 mm long could be grown (Figure 5 (a)). The crystallinity was checked by the Laue XRD method using back-reflection mode with the X-ray incident direction perpendicular to one of the small facets of the rods. Patterns shown in Figure 5 (b to g) were collected along the length of the crystal (from top to bottom) with an interval distance of about 8 mm. All diffraction patterns match the simulated pattern in the *c*-orientation (Figure 5 (d)) confirming that the grown rod is indeed a single crystal. The above reported single crystal diffraction data, clearly imply that the growth direction is perpendicular to the c-direction.

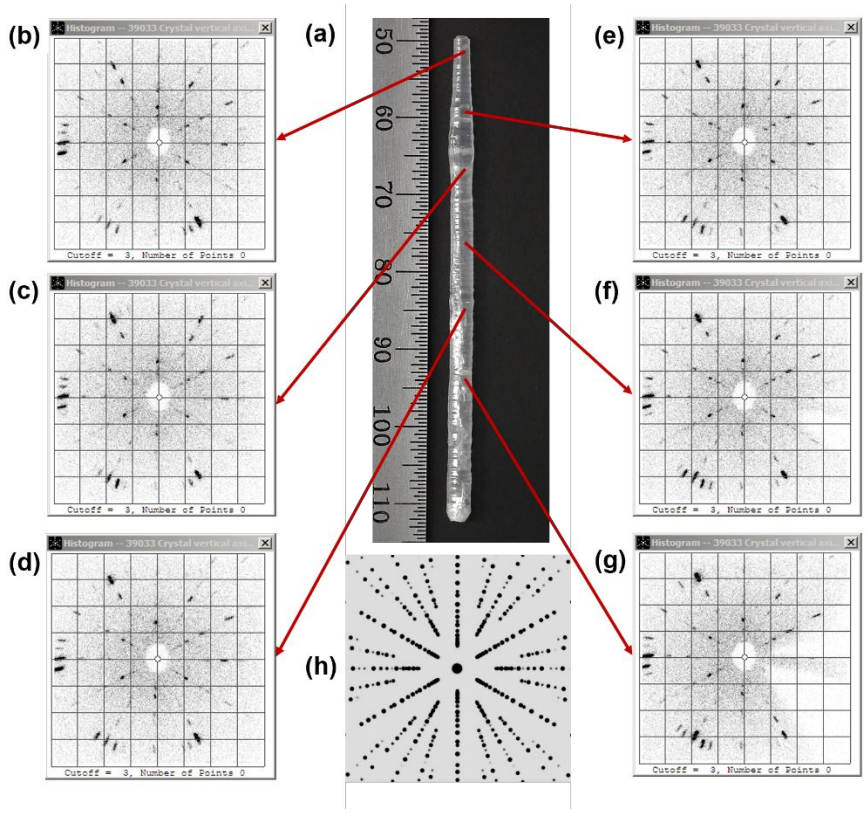

Figure 5. As-grown $Mg_4Ta_2O_9$ crystal rod (a) grown at 2 mm/h after modification of the furnace. Experimental X-ray Laue patterns taken perpendicular to the rod axis at different positions (b to g). Simulated X-ray Laue diffraction pattern along *c*-axis (h). Note: part of the pattern g was masked by the sample holder.

A common crack formation is shown in Figure 6. $Mg_4Ta_2O_9$ crystallizes in the trigonal group $P\bar{3}c1$ (165), with unit cell parameters a=5.1626(10) Å, c=14.035(4) Å (see supplement data Table S1). All tantalum atoms adopt octahedral coordination with two types of Ta-O bonding that have bond length of 1.899(3) Å and 2.118(3) Å, respectively. Each couple of TaO_6 octahedron connect internally via sharing edge, composing isolated layers in *ab*-plane. The magnesium atoms are coordinated by six oxygen atoms with Mg-O bond length of 2.023(2)-2.205(2) Å. A potential cleavage plane appears in the Mg-O-O-Mg-Mg-O plane along the growth direction.

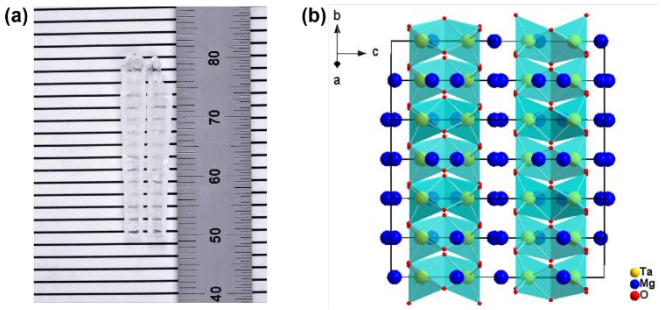

Figure 6. (a) Typical cracking appearance of $Mg_4Ta_2O_9$ rod grown by the floating-zone growth. (b) Atomic arrangement projected on the *bc* plane of $Mg_4Ta_2O_9$ crystal structure.

Scintillation Properties

X-ray luminescence and decay. The XRL spectrum of $Mg_4Ta_2O_9$ crystal measured at room temperature is shown in Figure 7(a), and presents a broad band with a maximum at about 3.4 eV. The emission can be fitted using two Gaussian components with centers at 3.45 eV and 3.05 eV, and a FWHM of 0.68 eV and 0.77 eV, respectively. The mechanism responsible for the intrinsic luminescence (3.45 eV, 359 nm) in $Mg_4Ta_2O_9$ was reported as a metal-to-ligand charge transition, where the excited state is the $5d^0$ state of tantalum and the ground state is the $2p^6$ state associated with the oxygen ligand [26]. Similar luminescence processes have been determined in other self-activated transition metal oxides, for example molybdates and tungstate [29,30]. The lower energy emission is likely related to oxygen vacancies [31].

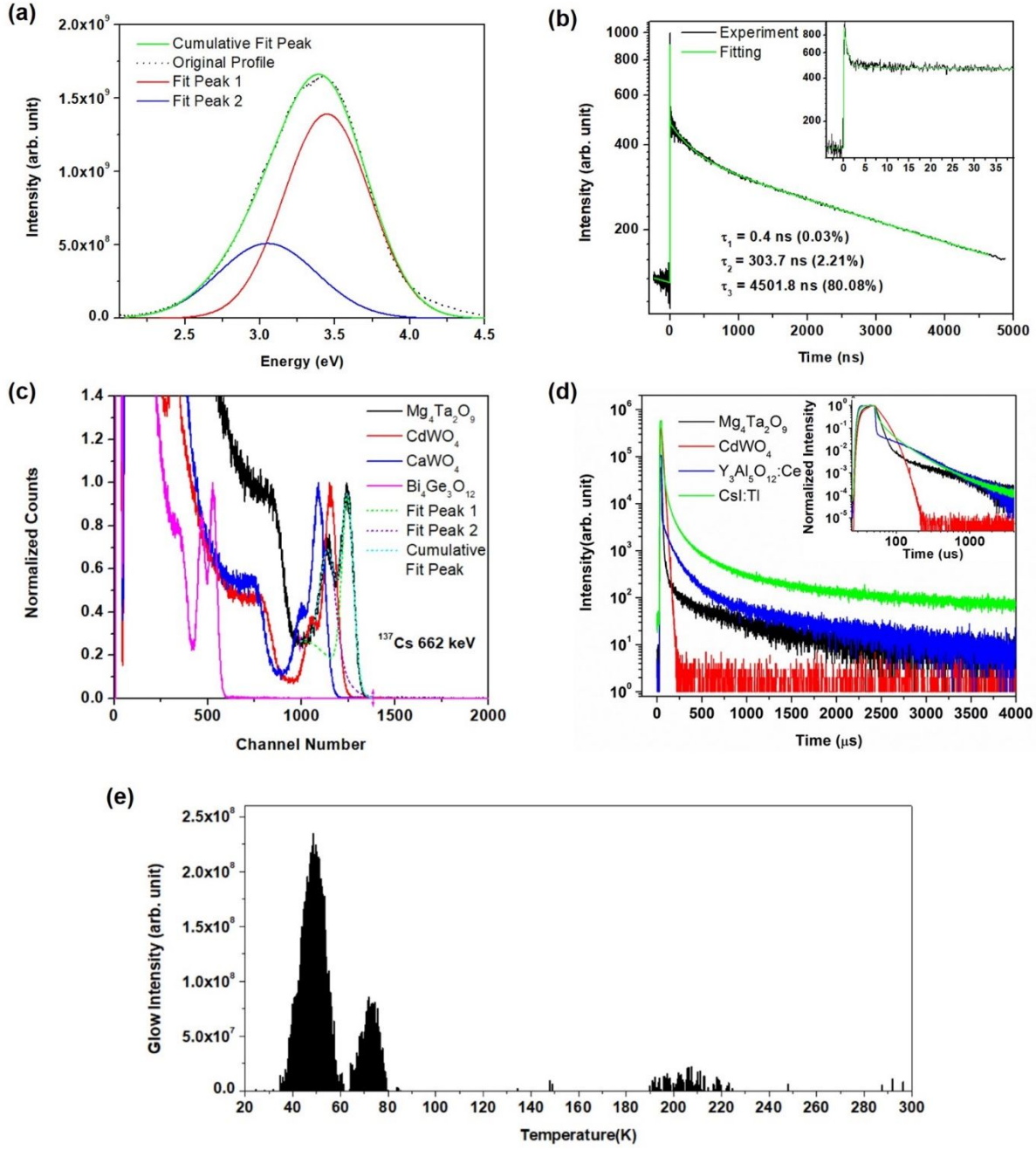

Figure 7. Room temperature (a) radio-luminescence spectrum and (b) scintillation decay curve of $Mg_4Ta_2O_9$ crystal. (c) Pulse height spectra of $Mg_4Ta_2O_9$ compared with $CdWO_4$, $CaWO_4$, and $Bi_4Ge_3O_{12}$. The dash lines are fit in terms of Gaussian components of the photopeak of $Mg_4Ta_2O_9$. (d) X-ray induced afterglow curves of $Mg_4Ta_2O_9$ crystal and $CdWO_4$, CsI:Tl, and $Y_3Al_5O_{12}$:Ce reference samples. The inset reports the same data normalized to their maxima and on a bi-log plot. (e) TSL glow curve of $Mg_4Ta_2O_9$ crystal.

Figure 7(b) reports the room temperature X-ray excited luminescence decay of $Mg_4Ta_2O_9$ single crystals and the inset is an enlargement of the decay profile within the first 40 ns. To analyze the decay profile, the curve is fitted with a multi-

exponential function, and the fit result is shown in the figure as well. The decay curve is well reconstructed by three exponential decay components with lifetimes of 0.4 ns, 303.7 ns, and 4501.8 ns, the last one accounting for 80 % of the total decay with a few per cent accuracy. Although the primary decay of $Mg_4Ta_2O_9$ is relatively long with respect to those of other tantalate compounds [12], it is still much faster than those of molybdates and tungstates (e.g., 16 µs for $CaMoO_4$ single crystals and 14 µs for $CdWO_4$ [32,33]).

Light yield and energy resolution. Light yields were estimated based on the gamma-ray excited photopeak of as-grown $Mg_4Ta_2O_9$ crystals and three references, $CdWO_4$, $CaWO_4$, and $Bi_4Ge_3O_{12}$. The $Mg_4Ta_2O_9$ samples were polished manually on both sides, with Al_2O_3 powders of different sizes until an optical finish was obtained. Several polished crystal plate samples (1.5 mm thick) are shown in figure 8.

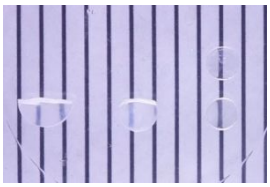

Figure 8. Photograph of $Mg_4Ta_2O_9$ crystal slices (polished on both sides) used for the light yield and energy resolution measurements. The black lines are separated by 1 mm.

The pulse height spectra can be found in Figure 7(c). The obvious double peak of $Mg_4Ta_2O_9$, is due to the escape of Ta Kα characteristic x-rays related to the sample small dimensions. At 662 keV, the light yield of $Mg_4Ta_2O_9$ is 13,000 ± 2,000 ph/MeV, with an energy resolution of 6%. The result is very similar to that reported previously in [12] for samples of similar sizes (disks cut perpendicular to the growth direction) indicating that the improved growth parameters do not strongly influence the light yield of these small samples. Samples from the first study were chosen free of cracks. Still the improved growth parameters enabled the growth of longer rods that appears free of macroscopic structural defects (bubbles/voids, cracks and inclusions) upon both visual inspection and optical microscopy of polished slices. This is crucial for imaging performances since macroscopic defects affect the diffusion and thus the spatial resolution.

Afterglow. A scintillator that rapidly decays to the lowest constant residual afterglow, allows a short veto time and a large collection rate of its scintillation for high-speed imaging applications [34]. As shown in Figure 7(d), the reference $CdWO_4$ exhibits the smallest afterglow level while CsI:Tl shows the largest afterglow signal when considering their absolute afterglow intensity. $CdWO_4$ is characterized by an afterglow lower than 0.01% / 3 ms. CsI:Tl and $Y_3Al_5O_{12}$:Ce have similar fairly large afterglow of about 0.1% at 2 ms, (see figure 7(d) inset). We have to note, though, that the CsI:Tl afterglow here reported appears to be optimistic compared to published afterglow data of about 2 % / 2 ms [35, 36]. The afterglow in the ms range of our $Mg_4Ta_2O_9$ scintillator crystal is similar to those of $Y_3Al_5O_{12}$:Ce and CsI:Tl. The normalized results reported in the figure inset in the time range 0 to 1200 µs show that $Mg_4Ta_2O_9$ has a much lower afterglow values in the 100-1,000 µs with respect to CsI:Tl, $Y_3Al_5O_{12}$:Ce, while $CdWO_4$ is limited by its long decay time. The afterglow is generally related to the presence of defects acting as traps for charge carriers and $Mg_4Ta_2O_9$ indeed shows two rather shallow traps evidenced in the thermally stimulated luminescence results in Figure 7(e). The full analysis of the TSL glow curves and their spectra are beyond the scope of the paper. Further developments in the growth of $Mg_4Ta_2O_9$, for instance by considering doping with monovalent or trivalent cations, will be explored in the future to control the intrinsic traps and reduce the afterglow of $Mg_4Ta_2O_9$ [37].

Comparative performance.

Table 1 lists the scintillation relevant properties of $Mg_4Ta_2O_9$ and those of three other commercial scintillators for comparative purpose. Although the afterglow of $Mg_4Ta_2O_9$ (0.011% at 3 ms) does not outperform $CdWO_4$, it is similar to those of $Y_3Al_5O_{12}$:Ce and CsI:Tl. $Mg_4Ta_2O_9$ has a Z_{eff} and density higher than that of CsI:Tl and its luminosity is similar to that of $CdWO_4$. $Mg_4Ta_2O_9$ is then seen as viable scintillator that does not contain any toxic material and could be developed further for radiography or other applications.

Table 1. Comparison of properties of $Mg_4Ta_2O_9$ with other commercial scintillators.

Crystal	$Mg_4Ta_2O_9$	$CdWO_4$ [39]	$Bi_4Ge_3O_{12}$ [40]	CsI:Tl [36,37]
Structure	Trigonal P $\bar{3}$c1	Monoclinic P 12/c1	Cubic I $\bar{4}$3d	Cubic Pm-3m
Density (g/cm^3)	6.2	7.9	7.1	4.5
Z_{eff}	59.6	64.2	75.1	54
Attenuation length at 662 keV (cm)	1.82	1.45	1.41	2.87
Emission wavelength (nm)	360	475	480	550
Light yield (ph/MeV)	11,000-15,000	12,000-15,000	8,000-10,000	52,000-56,000
Energy resolution	6 %	8.3 %	9 %	5.7 %
Primary decay time (ns)	4,500	14,000	300	1,000
Afterglow (/ms)	0.011% / 3	<0.01% / 3	0.015%/20	2% / 2

Conclusions

The modified floating-zone method reported here successfully solved the growth issues of $Mg_4Ta_2O_9$ bulk crystal that have been previously reported. Shallower thermal gradients during cooling prevented cracking and good quality crystal rods with sizes of the order of Φ3.5 mm × 50 mm could be obtained free of macroscopic structural defects. $Mg_4Ta_2O_9$ melts congruently and other growth techniques such as Czochralski could be attempted for growth of larger crystals.

The scintillation properties including radio-luminescence, decay time and afterglow were measured and compared to commercial scintillators $CdWO_4$, $Bi_4Ge_3O_{12}$, and CsI:Tl. As in the case of $CdWO_4$, $Mg_4Ta_2O_9$ is an intrinsic scintillator, which eliminates the possibility of inhomogeneity induced by dopant segregation in single crystals. The main advantage of $Mg_4Ta_2O_9$ over $CdWO_4$ is its lack of toxic element in its composition.

Conflicts of interest

There are no conflicts to declare.

Acknowledgements

The authors would like to thank Chris Rosen, Steve Hanrahan for their support of the experimental work and Prof. Stephen Derenzo for valuable discussions and suggestions. The single crystal X-ray diffraction measurements were done and analyzed by Dr. Guang Wu at the University of California Santa Barbara. This work was supported by the U.S. Department of Homeland Security/DNDO and was carried out at the Lawrence Berkeley National Laboratory under Contract no. DE-AC02-05CH11231.

Notes and references

Supporting Information. Table S1 reports crystal data and structure refinement parameters for $Mg_4Ta_2O_9$. CCDC 1855834 contains the supplementary crystallographic data for $Mg_4Ta_2O_9$.

1 Nondestructive Testing Handbook, 3rd Ed., Vol. 4, Bossi, R. H., Iddings, F. A., Wheeler, G. C., and Moore, P. O., eds. (Am. Soc. Nondestructive Testing, Columbus, Ohio, 2002).
2 Y. Liu, B. D. Sowerby and J. R. Tickner, *Applied Radiation and Isotopes*, 2008, **66**, 463-473.
3 P. Lecoq, Nuclear Instruments and Methods in Physics Research Section A: Accelerators, Spectrometers, Detectors and Associated Equipment, 2016, **809**, 130-139.
4 M. Nikl and A. Yoshikawa, *Advanced Optical Materials*, 2015, **3**, 463-481.
5 C. Dujardin, E. Auffray, E. Bourret-Courchesne, P. Dorenbos, P. Lecoq, M. Nikl, A. N. Vasil'ev, A. Yoshikawa and R. Zhu, *IEEE Transactions on Nuclear Science*, 2018, **65**, 1977-1997.
6 A. Annenkov, M. V. Korzhik and P. Lecoq, Nuclear Instruments and Methods in Physics Research Section A: Accelerators, Spectrometers, Detectors and Associated Equipment, 2002, **490**, 30-50.
7 M. Michail, G. P. Fountos, S. L. David, I. G. Valais, A. E. Toutountzis, N. E. Kalyvas, I. S. Kandarakis and G. S. Panayiotakis, *Measurement Science and Technology*, 2009, **20**, 104008.
8 Y. K. Kim, H. K. Kim, G. Cho and D. K. Kim, Nuclear Instruments and Methods in Physics Research Section B: Beam Interactions with Materials and Atoms, 2004, **225**, 392-396.
9 W. Wang, Y. Li, H. Kou, S. Liu, W. Liu, Y. Shi, J. Li, X. Feng, Y. Pan and J. Guo, *International Journal of Applied Ceramic Technology*, 2015, **12**, E249-E255.
10 V. V. Postupaev, Nuclear Instruments and Methods in Physics Research Section A: Accelerators, Spectrometers, Detectors and Associated Equipment, 2019, **923**, 147-156.
11 E. E. Ovechkina, V. Gaysinskiy, S. R. Miller, C. Brecher, A. Lempicki and V. V. Nagarkar, *Radiation Measurements*, 2007, **42**, 541-544.
12 E. D. Bourret, D. M. Smiadak, R. B. Borade, Y. Ma, G. Bizarri, M. J. Weber and S. E. Derenzo, *Journal of Luminescence*, 2018, **202**, 332-338.
13 L. Li, W. Liu, B. Han, X. Jin, F. Li, W. Wang, Q. Zhou, D. Xu and T. Cui, *RSC Advances*, 2015, **5**, 66988-66993.
14 Bulk Crystal Growth, Handbook of Crystal Growth, Elsevier, 2015, Pages 281-329.
15 S.M.Koohpayeh, D.Fort, J.S.Abell Progress in Crystal Growth and Characterization of Materials, Volume 54, Issues 3–4, September–December 2008, Pages 121-137
16 A. M. Balbashov, Crystals 2019, 9, 487.
17 M. A. Gonik, A. Cröll, CrystEngComm, 2013,15, 2287-2293
18 M. Hossain, S. Watauchi, M. Nagao and I. Tanaka, *CrystEngComm*, 2014, **16**, 4619-4623.
19 S. M. Koohpayeh, D. Fort and J. S. Abell, *Progress in Crystal Growth and Characterization of Materials*, 2008, **54**, 121-137.
20 S. M. Koohpayeh, J. J. Wen, M. Mourigal, S. E. Dutton, R. J. Cava, C. L. Broholm and T. M. McQueen, *Journal of Crystal Growth*, 2013, **384**, 39-43.
21 P. Hammersley, *FIT2D V9.129 Reference Manual V3.1*, Report ESRF98HA01T, ESRF Internal Report, 1998.
22 *K. Brandenburg and H. Putz, Match!*, 2.4.7; Crystal Impact: Bonn, Germany, 2007.
23 *SMART & SAINT Software Reference Manual*, 6.45; Bruker Analytical X-Ray Systems, Inc.: Madison, WI, 2003.
24 G. D. Antona, IEEE Transactions on Instrumentation and Measurement, 2003, **52**, 189-196.
25 G. M. Sheldricka, *Acta Crystallographica Section A*, 2008, **64**, 112-122.
26 G. M. Sheldrick, *SHELXTL*, Bruker Alalytical X-ray Systems Inc: Madison, WI, 2014.
27 C. Marín and E. Diéguez, Orientation of Single Crystals by Back-Reflection Laue Pattern Simulation, WORLD SCIENTIFIC, 1999.
28 S. Derenzo, G. Bizarri, R. Borade, E. Bourret-Courchesne, R. Boutchko, A. Canning, A. Chaudhry, Y. Eagleman, G. Gundiah, S. Hanrahan, M. Janecek and M. Weber, *Nuclear Instruments and Methods in Physics Research Section A: Accelerators, Spectrometers, Detectors and Associated Equipment*, 2011, **652**, 247-250.
29 G. Blasse and A. Bril, *Journal of Solid State Chemistry*, 1971, **3**, 69-74.
30 V. B. Mikhailik and H. Kraus, *physica status solidi (b)*, 2010, **247**, 1583-1599.
31 B. Ding, C. Han, J. Zhang, W. Chen, L. Ma and Z. Tang, *Science of Advanced Materials*, 2017, **9**, 306-315.
32 B. Ding, H. Qian, C. Han, J. Zhang, S.-E. Lindquist, B. Wei and Z. Tang, *The Journal of Physical Chemistry C*, 2014, **118**, 25633-25642.

33 S. B. Mikhrin, A. N. Mishin, A. S. Potapov, P. A. Rodnyi and A. S. Voloshinovskii, Nuclear Instruments and Methods in Physics Research Section A: Accelerators, Spectrometers, Detectors and Associated Equipment, 2002, **486**, 295-297.

34 L. Bardelli, M. Bini, P. G. Bizzeti, L. Carraresi, F. A. Danevich, T. F. Fazzini, B. V. Grinyov, N. V. Ivannikova, V. V. Kobychev, B. N. Kropivyansky, P. R. Maurenzig, L. L. Nagornaya, S. S. Nagorny, A. S. Nikolaiko, A. A. Pavlyuk, D. V. Poda, I. M. Solsky, M. V. Sopinskyy, Y. G. Stenin, F. Taccetti, V. I. Tretyak, Y. V. Vasiliev and S. S. Yurchenko, *Nuclear Instruments and Methods in Physics Research Section A: Accelerators, Spectrometers, Detectors and Associated Equipment*, 2006, **569**, 743-753.

35 S. C. Thacker, B. Singh, V. Gaysinskiy, E. E. Ovechkina, S. R. Miller, C. Brecher and V. V. Nagarkar, *Nucl Instrum Methods Phys Res A*, 2009, **604**, 89-92.

36 Saint-Gobain Crystals: CsI(Tl), CsI(Na) Cesium Iodide, https://www.crystals.saint-gobain.com/products/csitl-cesium-iodide-thallium, (accessed July 16, 2018).

37 P. Bhattacharya, S. Miller, M. Wart, C. Brecher and V. V. Nagarkar, Bridgman-grown CsI:Tl crystals codoped to suppress afterglow for high-throughput cargo inspection, SPIE, 2018.

38 L. Nagornaya, G. Onyshchenko, E. Pirogov, N. Starzhinskiy, I. Tupitsyna, V. Ryzhikov, Y. Galich, Y. Vostretsov, S. Galkin and E. Voronkin, *Nuclear Instruments and Methods in Physics Research Section A: Accelerators, Spectrometers, Detectors and Associated Equipment*, 2005, **537**, 163-167.

39 G. Okada, M. Akatsuka, K. H., M. Mori, N. Kawano, N. Kawaguchi and T. Yanagida, *Sens. Mater.,* 2018, **30**, 1547-1554.

40 Saint-Gobain Crystals: CdWO4 Cadmium Tungstate, https://www.crystals.saint-gobain.com/products/cdwo4-cadmium-tungstate, (accessed July 16, 2018).

41 Saint-Gobain Crystals: BGO Bismuth Germanate, https://www.crystals.saint-gobain.com/products/bgo, (accessed July 16, 2018).